Mechanical Systems and Signal Processing 116 (2019) 816–831

Contents lists available at ScienceDirect

Mechanical Systems and Signal Processing

journal homepage: www.elsevier.com/locate/ymssp

Base-isolated structure equipped with tuned liquid column damper: An experimental study

Thomas Furtmüller [a,*], Alberto Di Matteo [b], Christoph Adam [a], Antonina Pirrotta [b,c]

[a] Unit of Applied Mechanics, University of Innsbruck, Technikerstr. 13, Innsbruck, Austria
[b] Dipartimento di Ingegneria Civile, Ambientale, Aerospaziale, dei Materiali (DICAM), Università degli Studi di Palermo, Viale delle Scienze, Palermo, Italy
[c] Department of Mathematical Sciences, University of Liverpool, UK

ARTICLE INFO

Article history:
Received 31 January 2018
Received in revised form 18 June 2018
Accepted 23 June 2018

Keywords:
Base-isolated structure
Tuned liquid column damper
Optimal design
Hybrid control strategy
Small-scale experiment

ABSTRACT

In this study, a novel passive vibration control strategy is investigated experimentally, where a Tuned Liquid Column Damper protects a base-isolated structure. The Tuned Liquid Column Damper is attached to the base, in contrast to typical attachment points of passive energy dissipation devices in high-rise buildings at elevated levels. Experiments on a base-excited small-scale three-story shear frame are conducted in order to study effects of both control devices – base-isolation and Tuned Liquid Column Damper – on the structural model. The dynamic properties of the stand-alone shear frame and the base-isolation subsystem are derived using standard dynamic test methods based on displacement and acceleration response measurements. In the base-isolation subsystem both viscous damping and friction effects are identified. The water level of the Tuned Liquid Column Damper is tracked by means of computational image processing of video recordings, facilitating the identification of the fundamental liquid motion mode as well as the nonlinear damping properties. An experimental parametric study is conducted for three Tuned Liquid Column Damper devices with different frequency tuning ratios. The assessment of the hybrid control strategy is based on the determined transfer functions of the studied setups. Experimental outcomes confirm recent theoretical findings that a passive hybrid control strategy combining a base-isolation and a Tuned Liquid Column Damper reduces the displacement demand of the base-isolation subsystem as well as the total story acceleration demand if both control devices are properly tuned.

1. Introduction

Control system approaches for vibration mitigation in civil structures can be classified into passive control, semi-active control, active control, and hybrid control strategies [1]. Semi-active and active control devices (and also the hybrid ones when active/semi-active schemes are involved) rely on a control algorithm, where either a variable damper property or a variable control force is adjusted, based on the identification of the structural vibration behavior. In contrast, passive control strategies are characterized by a fixed set of control parameters. Since passive systems cannot self-adjust to varying structural and/or excitation parameters, it is crucial that for these systems optimal control parameters are employed to achieve reliable vibration mitigation. Although from this point of view active or semi-active control systems seem to have superior

* Corresponding author.
E-mail address: thomas.furtmueller@uibk.ac.at (T. Furtmüller).

https://doi.org/10.1016/j.ymssp.2018.06.048
0888-3270/

performance properties, passive control devices are still the primary choice in engineering applications. They are more robust since they do not rely on additional external energy supply. During typical dynamic loading scenarios such as earthquake excitation a reliable external energy supply cannot be ensured. Additionally, passive devices are usually cheaper in installation and maintenance. Because for civil structures critical vibration states are often related to a specific vibrational mode that in many structures only varies slightly over time, a fixed optimal control strategy related to this mode is sufficient to reduce the dynamic response significantly.

Two passive control systems frequently used to mitigate earthquake induced structural vibrations are seismic base-isolation devices and tuned vibration absorbers. The concept of a base-isolation corresponds to the application of a low-pass filter to the earthquake ground motion. This is accomplished by means of laterally extremely flexible and vertically almost rigid devices, such as reinforced rubber bearings or frictional sliding elements, arranged between foundation and base of the load-bearing structure. In this manner, the natural frequency of the base-isolation subsystem ω_b serves as fundamental frequency of the controlled structure, whereas the fundamental frequency of the stand-alone structure is shifted to a higher value, depending on the mass ratio [2]. Furthermore, the first mode shape approaches a rigid body mode where most of the deformation is concentrated in the base-isolation. Thus, the main parameter influencing the efficacy of a base-isolation is frequency ω_b.

The tuned liquid column damper (TLCD) is an innovative absorber, where a oscillating liquid column inside a U-shaped container dissipates structural vibrations. The efficacy of a TLCD depends on its natural frequency and equivalent damping ratio optimally tuned to the parameters of the main structure. For a wide variety of different excitation signals and optimization criteria, optimal tuning parameters were derived [3]. In [4], the performance of a TLCD mounted on a spatial one-story frame was investigated experimentally, varying the excitation direction. Generally it is observed that the reduction of the dynamic amplification of the main structure increases with increasing ratio of effective TLCD mass to effective structural mass. In practical application, this mass ratio is limited to about 5%. As such, the efficacy of the TLCD is based on the same mechanical principle as the classical tuned mass damper (TMD), however the TLCD has some advantages compared to the TMD [5]. For instance, it is a low cost device easy to implement, fine tuning of the TLCD frequency can be conducted by simply adding or removing some liquid, and maintenance of this device is straightforward because no elaborate mechanical components are involved. The fundamental frequency of a TLCD with constant cross-section depends on the length of the liquid column only. Thus, a TLCD can be used to mitigate vibrations of structures with a fundamental frequency less than approximately 2 Hz because the column length cannot be reduced below a certain value.

As a drawback, a base-isolation subsystem may be subjected to excessive large dynamic displacement demands, and consequently, it must resist those large deformations, which can be a limiting design factor. To overcome this limitation, a passive hybrid control strategy has been proposed, composed of a base-isolation subsystem and a tuned vibration absorber, see e.g. [7,8]. The principal idea is to reduce the displacement demand of the base-isolation subsystem by application of an absorber tuned to the natural frequency of the base-isolation subsystem. The absorber is directly attached to the base, and as such the dead weight does not stress the main structure as encountered in a solely tuned vibration absorber-controlled structure. In the large majority of the studies (for instance [8,7,9–11]), a TMD was used as vibration absorber. In the context of taking into account the beneficial properties of the TLCD, in [6] the effect of a TLCD on a base-isolated five-story frame structure was studied numerically, and in [12] a novel base-isolation control system with increased effective damping supplied by a TLCGD was proposed. Recently, the authors of the present contribution investigated in detail the control performance of a TLCD on the seismic response of a base-isolated multi-degree-of-freedom (MDOF) frame structure [13]. They proposed a straightforward procedure for direct evaluation of the equivalent linear TLCD parameters. Based on this procedure, and assuming that the base-isolated load-bearing structures behaves rigid, a direct optimization procedure of the TLCD design parameters was performed, aiming at maximum control of the seismic response of base-isolated frame structures.

Although a large number of papers exist on theoretical considerations based on numerical simulations, application and experimental verification of the performance of a TLCD respectively seismic base-isolation in combination with other control devices is scarce. For instance, in [14] the outcomes of experimental tests on a small-scale shear frame equipped with a TLCD, however, without base-isolation subsystem, are presented. In [15,19] the investigation of a TLCD attached to a single-story frame model verified experimentally that a numerical procedure proposed in [16–18] is capable of predicting the response of both the main structure as well as of the TLCD. A new type of tuned liquid damper was validated experimentally in [20]. Experiments on base-isolated structures were conducted in [21], with particular emphasis on revealing the performance of viscous and elastic-plastic damper devices. In [22] the effects of the frequency tuning ratio on the dynamic response of a base-isolated structure controlled by a TMD system were studied experimentally, using a pendulum with adjustable length as TMD.

To the best knowledge of the authors, no experimental verification of the effect of a TLCD device on a base-isolated structure is available. Therefore, in this contribution for the first time this passive hybrid control strategy is investigated experimentally on a small-scale three-story model frame, with the main goal of examining both dissipation mechanisms, base-isolation and TLCD device. The present experimental study complements the numerical considerations of [13], thus, putting theory and application in one framework. The paper is organized as follows. At first, the experimental setup is described, and the corresponding analytical model for comparative numerical studies is established. Then, the identification of the structural parameters of each subsystem – stand-alone shear frame, base-isolation subsystem, and TLCD device – is described and nonlinear effects are assessed. Experiments on the base-isolated small-scale model are conducted, considering three

different TLCD setups, and for comparison without TLCD control. Finally, the outcomes of comparative numerical studies, which are based on the previously identified subsystem parameters, are set in contrast to the experimentally derived ones.

2. Experimental setup

2.1. Test specimen

The studied test specimen is a planar base-isolated single-bay three-story shear frame equipped with a TLCD at the base, as shown in Fig. 1. The width of the frame is 28 cm, and its total height is 65 cm, thus representing an approximate 1:20 scale model of a shear building. The clear floor height of the first story is 17.3 cm, of the second story 14.4 cm, and of the third story 17.0 cm. The horizontal beams of the base and of the three story levels are made of aluminum profiles with cross-section 40×40 mm, and they can be considered as rigid in the applied range of frequencies. In contrast, the aluminum columns with rectangular cross-sections (width 40 mm, thickness 2 mm) allow for flexibility, and they are clamped to the horizontal beams by quasi-rigid aluminum plates.

The beam at the base of the frame (referred to as base beam) is bolted to the upper base plate (aluminum alloy, dimension $35 \times 35 \times 1$ cm) of the base-isolation subsystem, which is depicted in Fig. 2(a). The bottom plate (aluminum alloy, dimension $35 \times 35 \times 1$ cm) represents the foundation of the model. The bottom and the base plate are separated by two pairs of guidance beams arranged in parallel to the frame plane, one pair to the left, and the second pair to the right of the planar frame structure. The external beams (in Fig. 2(a) referred to as G1) of these pairs are rigidly connected to the base plate, whereas the internal beams (referred to as G2) are fixed to the bottom plate. Two steel spheres in-between each pair of guidance beams facilitate the desired relative uniaxial horizontal motion between the plates. In Fig. 2(b) a section representing a sketch of the sliding mechanism is shown. Four extension springs, which connect the guidance beams G1 and the bottom plate at each end, provide the stiffness of the base-isolation subsystem. It is possible to deactivate the base-isolation for comparative experiments by two screws (in Fig. 2(a) referred to as S1 and S2), which allow to connect both plates quasi rigidly.

The U-shaped container of the TLCD is made of acrylic glass pipes with circular cross-section. The inner diameter of the pipes with 2 mm wall thickness is 26 mm, the total horizontal length of the TCLD is 24 cm, and its total height is 13 cm. The container is filled with water colorized by blue dye to enhance the contrast. In the experiments studying the response of the hybrid-controlled system, the TLCD subsystem is mounted to the base beam. Fig. 2(c) shows a close-up photo of the TLCD attached to the base-isolated structure.

The complete test specimen, developed at the Unit of Applied Mechanics, University of Innsbruck, rests on two linear bearings, thus confining its motion to a horizontal uniaxial one in the direction of the frame plane. An APS 400 Electro-Seis long-stroke shaker manufactured by *APS Dynamics, Inc.*, connected via a stinger rod to the bottom plate, imposes the desired ground excitation.

For signal generation and data acquisition, a *National Instruments* CompactDAQ (NI cDAQ) system controlled by a MATLAB script is used. Two optical laser sensors of type optoNCDT 1320–100 manufactured by *Micro-Epsilon Messtechnik GmbH* record the displacements of the bottom and the base plate with respect to a quasi-rigid vertical support bar. In Fig. 1, the

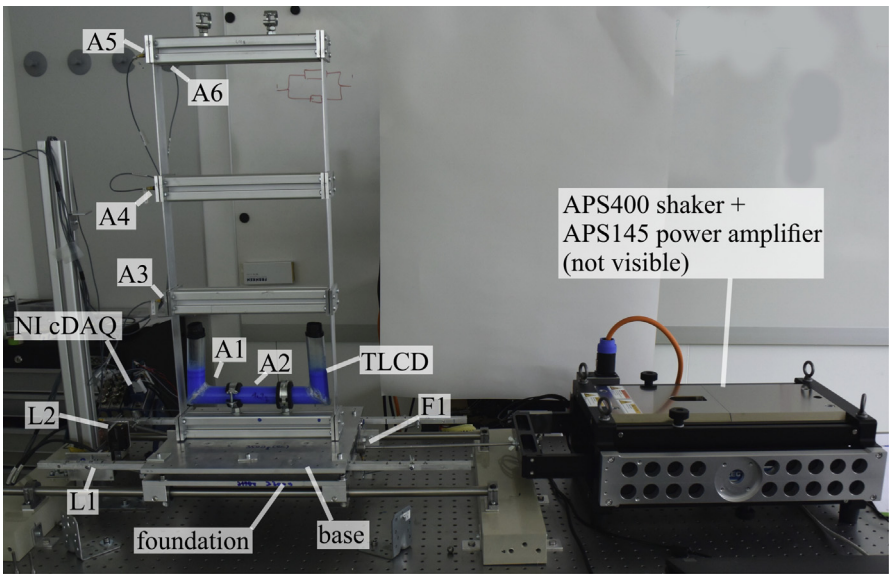

Fig. 1. Test setup with sensor locations A1 to A6.

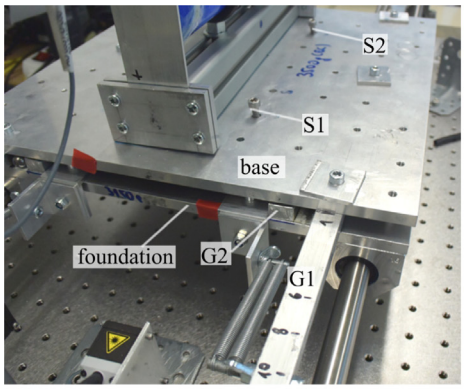

(a) Base-isolation subsystem

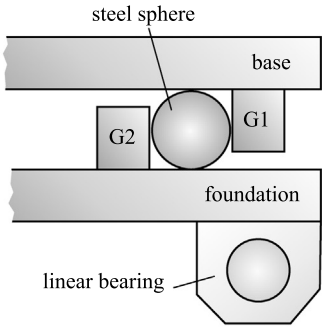

(b) Sketch of the sliding mechanism (not in scale)

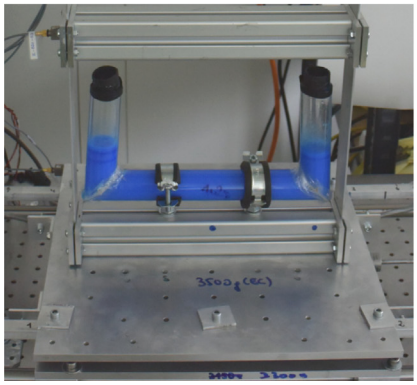

(c) TLCD device

Fig. 2. Detailed view of the control devices.

laser sensors are denoted as L1 and L2. Six uniaxial piezoelectric accelerometers of type DeltaTron 4508B (*Brüel & Kjær*) are attached to the system at locations denoted as A1 to A6 in Fig. 1. They record the total accelerations of the bottom and the base plate, the three story beams, and the out-of plane acceleration of the top story. Note that sensors A1 and A2 not visible in Fig. 1 measure accelerations in the same directions as sensors A3, A4 and A5.

2.2. Excitation signal

The effect of the proposed hybrid control strategy is investigated on structural configurations subjected to white noise ground excitation. Since no closed-loop control system is available, the corresponding excitation signal is generated in a two-step procedure. In the first step, a band-limited pseudo-random signal exhibiting a unit amplitude and uniformly distributed random phase in the frequency-domain is used as input voltage signal $u_0(t)$ to excite the test specimen. The acceleration of the bottom plate $\ddot{x}_g(t)$ recorded in this pilot experiment is the output signal. Power spectral densities (PSDs) are computed for both, the input and output signal. Assuming linear system behavior, these PSDs are related via a transfer function $H_{\ddot{x}U}(f)$ [23]. As amplitudes of this transfer function are readily obtained, its inverse $|H_{\ddot{x}U}(f)|^{-1}$ is used to correct the amplitudes of the pseudo-random input signal, resulting in a new voltage signal $u_1(t)$ that is sent via the power amplifier to the shaker. Then, the acceleration of the bottom plate recorded during the experiment is supposed to match the targeted band-limited white noise signal.

As an example, this excitation signal generation procedure is tested on the specimen with deactivated control devices. The targeted band-limited white noise excitation signal with lower and upper cut-off frequencies of $f_u = 5$ Hz respectively $f_o = 50$ Hz cover the range of natural frequencies of the considered specimen configuration (see Section 3.1) The result of this procedure is shown in Fig. 3, where the black solid line represents the PSD of the corrected input voltage signal denoted as $S_{U,1}(f)$. The red dashed graph refers to the PSD $S_{\ddot{x}}(f)$ of the recorded ground acceleration of the specimen subjected to the shaker force, which is driven by the time-history signal $u_1(t)$. It is readily observed that the derived ground acceleration matches closely the targeted band-limited white noise excitation with constant PSD $S_{\ddot{x}}(f)$ in the considered frequency range

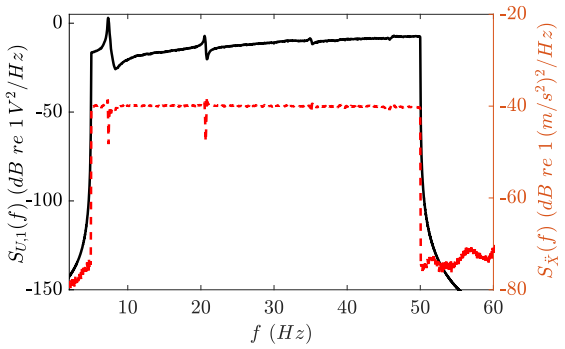

Fig. 3. Power Spectral Density of band-limited white noise excitation. Input voltage signal (black graph) and resulting ground acceleration signal (red graph). (For interpretation of the references to colour in this figure legend, the reader is referred to the web version of this article.)

except for minor deviations at three distinct frequencies. As shown later, these frequencies correspond to the natural frequencies of the considered stand-alone three-story frame without control devices. In the subsequent investigations, transfer functions are based on measured both input and output signals. Thus, as long as the test specimen does not exhibits pronounced nonlinearities, application of this approximated band-limited white noise signal as excitation yields transfer functions close to the ones based on perfect white noise excitation.

2.3. Analytical model and equations of motion

Results of numerical response analyses, which are set in contrast to the experimental outcomes, are based on the analytical model of the hybrid-controlled test specimen depicted in Fig. 4. At first, the equations of motion of this model are specified for the subsystems TLCD, shear frame, and base-isolation separately.

When subjected to base motion $x_b(t)$, the liquid column (horizontal length L_H, height L_V) of the TLCD can be described by a single-degree-of-freedom (SDOF) oscillator. The equation of motion, written in terms of the relative mean liquid surface displacement y, reads as [24]

$$\ddot{y} + \frac{\xi}{2L_{eff}}|\dot{y}|\dot{y} + \omega_l^2 y + \alpha\ddot{x}_b = 0,\ \ \omega_l = \sqrt{2g/L_{eff}} \tag{1}$$

Here, ξ is a loss factor dependent on the type of flow, ω_l denotes the natural circular frequency of TLCD oscillation, g is the gravitational acceleration, and $L_{eff} = 2L_V + L_H$ is the total length of the liquid column. The participation factor on the right-hand side of Eq. 1, $\alpha = L_H/L_{eff}$, describes the ratio of effectively moving liquid in horizontal direction, m_{lH}, to the total liquid mass, m_l. Linearization of nonlinear damping apparent in Eq. 1 yields

$$\ddot{y} + 2\zeta_l\omega_l\dot{y} + \omega_l^2 y + \alpha\ddot{x}_b = 0 \tag{2}$$

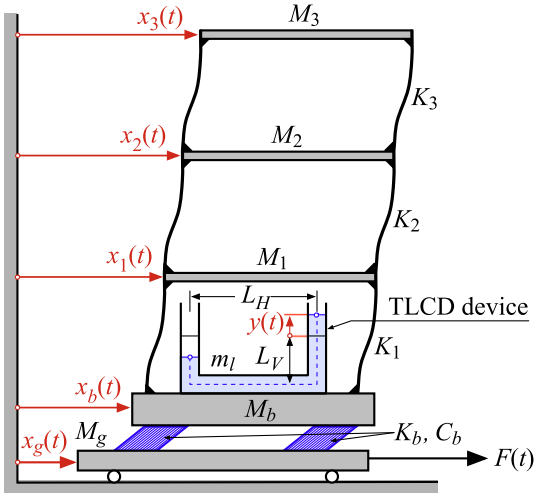

Fig. 4. Sketch of the hybrid-controlled system.

representing a linear viscously damped SDOF oscillator with scaled base excitation. Different approaches are available to derive the equivalent viscous damping ratio ζ_l, such as the method of harmonic balance [25] or statistical linearization [26].

Modeling of the three-story shear frame is based on the assumption that the beams are rigid and the columns perfectly elastic. Story masses and story stiffness coefficients are denoted as M_i respectively $K_i, i = 1,2,3$. The stand-alone shear frame has three degrees-of-freedoms (DOFs) and its vibrations are described by the horizontal displacements $x_i, i = 1,2,3$ of the beams. Since in the experiment total displacements and accelerations are recorded, x_i are absolute coordinates (i.e. measured with respect to the inertial system). The equations of motion of the frame substructure subjected to base displacement x_b (which is also an absolute coordinate) read as

$$\begin{bmatrix} M_1 & 0 & 0 \\ 0 & M_2 & 0 \\ 0 & 0 & M_3 \end{bmatrix} \begin{Bmatrix} \ddot{x}_1 \\ \ddot{x}_2 \\ \ddot{x}_3 \end{Bmatrix} + \begin{bmatrix} c_{11} & c_{12} & 0 \\ c_{21} & c_{22} & c_{23} \\ 0 & c_{32} & c_{33} \end{bmatrix} \begin{Bmatrix} \dot{x}_1 \\ \dot{x}_2 \\ \dot{x}_3 \end{Bmatrix} + \begin{bmatrix} K_1+K_2 & -K_2 & 0 \\ -K_2 & K_2+K_3 & -K_3 \\ 0 & -K_3 & K_3 \end{bmatrix} \begin{Bmatrix} x_1 \\ x_2 \\ x_3 \end{Bmatrix} + \begin{Bmatrix} c_{1b} \\ 0 \\ 0 \end{Bmatrix} \dot{x}_b + \begin{Bmatrix} -K_1 \\ 0 \\ 0 \end{Bmatrix} x_b = \begin{Bmatrix} 0 \\ 0 \\ 0 \end{Bmatrix} \tag{3}$$

Assuming that damping of the stand-alone frame structure can be captured according to Rayleigh damping, i.e. the damping matrix is proportional to the mass matrix and the stiffness matrix [27], the following elements of the damping matrix are derived,

$$c_{11} = \eta M_1 + \beta(K_1 + K_2),\ c_{12} = c_{21} = -\beta K_2,\ c_{22} = \eta M_2 + \beta(K_2 + K_3)\ , c_{23} = c_{32} = -\beta K_3,\ c_{33} = \eta M_3 + \beta K_3,\ c_{1b} = -\beta K_1 \tag{4}$$

where η is the mass-proportional and β the stiffness-proportional Rayleigh coefficient.

Between the rigid base plate (mass M_b) below the shear frame and the rigid bottom plate (mass M_g), a linear elastic spring (stiffness K_b) and a viscous damper (coefficient C_b) arranged in parallel capture the flexibility of the base-isolation subsystem. As such, an additional DOF is imposed to the system, expressed through the total base displacement x_b, governed by the following equation of motion,

$$(M_b + m_l)\ddot{x}_b + \alpha m_l \ddot{y} + \sum_{i=1}^{3} M_i \ddot{x}_i + C_b(\dot{x}_b - \dot{x}_g) + K_b(x_b - x_g) = 0 \tag{5}$$

Since the desired ground acceleration $\ddot{x}_g$ is imposed to the bottom plate via a shaker, a force F subjected to the base plate excites the experimental model. Consequently, when prescribing in the analytical model force F, ground displacement x_g is also a DOF,

$$M_g \ddot{x}_g + (M_b + m_l)\ddot{x}_b + \alpha m_l \ddot{y} + \sum_{i=1}^{3} M_i \ddot{x}_i = F(t) \tag{6}$$

Combining the equations of motion of the subsystems (Eqs. (2)–(6)) yields the governing equations of the analytical model with six DOF,

$$\begin{bmatrix} M_g & M_b+m_l & \alpha m_l & M_1 & M_2 & M_3 \\ 0 & M_b+m_l & \alpha m_l & M_1 & M_2 & M_3 \\ 0 & \alpha m_l & m_l & 0 & 0 & 0 \\ 0 & 0 & 0 & M_1 & 0 & 0 \\ 0 & 0 & 0 & 0 & M_2 & 0 \\ 0 & 0 & 0 & 0 & 0 & M_3 \end{bmatrix} \begin{Bmatrix} \ddot{x}_g \\ \ddot{x}_b \\ \ddot{y} \\ \ddot{x}_1 \\ \ddot{x}_2 \\ \ddot{x}_3 \end{Bmatrix} + \begin{bmatrix} 0 & 0 & 0 & 0 & 0 & 0 \\ -C_b & C_b & 0 & 0 & 0 & 0 \\ 0 & 0 & 2\zeta_l\omega_l m_l & 0 & 0 & 0 \\ 0 & c_{1b} & 0 & c_{11} & c_{12} & 0 \\ 0 & 0 & 0 & c_{21} & c_{22} & c_{23} \\ 0 & 0 & 0 & 0 & c_{32} & c_{33} \end{bmatrix} \begin{Bmatrix} \dot{x}_g \\ \dot{x}_b \\ \dot{y} \\ \dot{x}_1 \\ \dot{x}_2 \\ \dot{x}_3 \end{Bmatrix}$$
$$+ \begin{bmatrix} 0 & 0 & 0 & 0 & 0 & 0 \\ -K_b & K_b & 0 & 0 & 0 & 0 \\ 0 & 0 & \omega_l^2 m_l & 0 & 0 & 0 \\ 0 & -K_1 & 0 & K_1+K_2 & -K_2 & 0 \\ 0 & 0 & 0 & -K_2 & K_2+K_3 & -K_3 \\ 0 & 0 & 0 & 0 & -K_3 & K_3 \end{bmatrix} \begin{Bmatrix} x_g \\ x_b \\ y \\ x_1 \\ x_2 \\ x_3 \end{Bmatrix} = \begin{Bmatrix} F \\ 0 \\ 0 \\ 0 \\ 0 \\ 0 \end{Bmatrix} \tag{7}$$

Note that the stiffness matrix of this set of equation is singular, because it includes a rigid body mode. Alternatively, Eqs. 7 can be expressed as base-excited system in terms of five DOFs, i.e. coordinates x_b, x_1, x_2, x_3 relative to ground and base, respectively, and y, as in [13]. In such formulation, the stiffness matrix is non-singular. In the present study, however, the vibrations are described by means of absolute coordinates according to Eqs. 7, because in the experiments absolute values are recorded (i.e., total accelerations, total displacements, and shaker force).

3. System identification

System identification procedures are applied to derive the parameter for the analytical model of the hybrid-controlled system. These parameters are identified for each subsystem separately, as described in the following.

3.1. Shear frame subsystem

For identification of the structural frame parameters, the experimental model with deactivated base-isolation and dismounted TLCD is subjected to band-limited white noise ground acceleration $\ddot{x}_g$, as described in Section 2.2. In the experiment, ground acceleration $\ddot{x}_g$, induced in-plane responses of the story beams $\ddot{x}_1, \ddot{x}_2$ and $\ddot{x}_3$, and a possible out-plane acceleration of the roof are recorded. Additionally, Laser sensor L1 picks up the ground displacement x_g. After the experiment, the in-plane response transfer function at each story level is determined by application of MATLAB function *tfestimate* [28] to the recorded accelerations. In function *tfestimate* the classical H_1 estimator [23] is implemented, which is based on Welch's averaged periodogram method [29]. To this end, the recorded time domain data (e.g. $\ddot{x}_j(t)$) are transferred into the frequency domain ($\ddot{X}_j(f)$), and the auto-spectral power density $S_{\ddot{X}_j\ddot{X}_j}(f)$ of input signal $\ddot{X}_j(f)$ and the cross-spectral power density $S_{\ddot{X}_k\ddot{X}_j}(f)$ between output $\ddot{X}_k$ and input $\ddot{X}_j$ are derived. Ratio $S_{\ddot{X}_j\ddot{X}_j}/S_{\ddot{X}_k\ddot{X}_j}(f)$ represents H_1, which is an approximation of transfer function $H_{\ddot{X}_j\ddot{X}_k}(f)$. For the transfer functions of the shear frame, the ground acceleration $\ddot{X}_g(f)$ is the input signal, and acceleration responses $\ddot{X}_i(f)$ $(i = 1, 2, 3)$ of the beams are the output signals. Thus, the transfer functions determined in this manner are denoted as $H_{\ddot{X}_i\ddot{X}_g}, i = 1, 2, 3$. Additionally, also the transfer function of the out-of-plane roof response is derived and it is referred to as $H_{\ddot{X}_o\ddot{X}_g}$. These transfer functions are shown in Fig. 5(a). As observed, in-plane transfer functions $H_{\ddot{X}_1\ddot{X}_g}, H_{\ddot{X}_2\ddot{X}_g}$ and $H_{\ddot{X}_3\ddot{X}_g}$ exhibit three distinct peaks at frequencies $f_1^s = 7.4$ Hz, $f_2^s = 20.7$ Hz and $f_3^s = 35.1$ Hz. Dynamic amplifications at those natural frequencies of the planar three-story frame are 43 dB, 34 dB and 26 dB, which correspond to amplification factors of approximately 100, 50 and 20, respectively. Anti-resonances occur at frequencies of 11.2 Hz, 15.6 Hz, and 29.2 Hz. The transfer function of the out-of plane roof acceleration $H_{\ddot{X}_o\ddot{X}_g}$, induced by unavoidable imperfections in the test setup, shows two natural frequencies at 15.6 Hz and 46.2 Hz. Since these out-of-plane modes are not closely spaced to the in-plane modes, consideration of the experimental setup as planar shear frame is justified. Note that the dynamic peak amplifications of $H_{\ddot{X}_o\ddot{X}_g}$ at the in-plane natural frequencies is in the order of magnitude of the transverse sensitivity of the sensors used, given as less than 5% of the reference sensitivity in the specifications.

Subsequently, based on these in-plane response transfer functions $H_{\ddot{X}_1\ddot{X}_g}, H_{\ddot{X}_2\ddot{X}_g}$ and $H_{\ddot{X}_3\ddot{X}_g}$ of the experimental setup, the parameters of the corresponding analytical shear frame model with deactivated base isolation and dismounted TLCD, whose vibration are described by the following set of equations,

$$\begin{bmatrix} M_g+M_b & M_1 & M_2 & M_3 \\ 0 & M_1 & 0 & 0 \\ 0 & 0 & M_2 & 0 \\ 0 & 0 & 0 & M_3 \end{bmatrix} \begin{Bmatrix} \ddot{x}_g \\ \ddot{x}_1 \\ \ddot{x}_2 \\ \ddot{x}_3 \end{Bmatrix} + \begin{bmatrix} 0 & 0 & 0 & 0 \\ c_{1g} & c_{11} & c_{12} & 0 \\ 0 & c_{21} & c_{22} & c_{23} \\ 0 & 0 & c_{32} & c_{33} \end{bmatrix} \begin{Bmatrix} \dot{x}_g \\ \dot{x}_1 \\ \dot{x}_2 \\ \dot{x}_3 \end{Bmatrix} + \begin{bmatrix} 0 & 0 & 0 & 0 \\ -K_1 & K_1+K_2 & -K_2 & 0 \\ 0 & -K_2 & K_2+K_3 & -K_3 \\ 0 & 0 & -K_3 & K_3 \end{bmatrix} \begin{Bmatrix} x_g \\ x_1 \\ x_2 \\ x_3 \end{Bmatrix} = \begin{Bmatrix} F \\ 0 \\ 0 \\ 0 \end{Bmatrix} \tag{8}$$

are identified. To this end, Eq. (8) are transformed into the frequency domain, frequency response functions $X_g(f), X_i(f), i = 1, 2, 3$ due to force $F(f)$ at the foundation are derived. The ratio of the ith story response $X_i(f)$ to the ground and $X_g(f)$ yields transfer function $\overline{H}_{X_iX_g}(f)$, equivalent to $H_{\ddot{X}_i\ddot{X}_g}$,

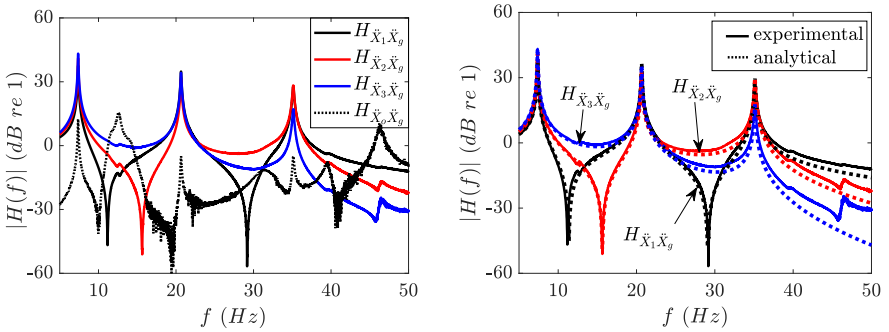

(a) Experimental outcomes. In-plane story and out-of-plane roof responses (b) Experimental versus analytical outcomes

Fig. 5. Story acceleration transfer functions of the standalone three-story frame with respect to the ground acceleration.

$$\overline{H}_{X_i X_g}(f) = X_i(f)/X_g(f), \quad i = 1,2,3 \tag{9}$$

The objective that resonances and anti-resonances of the experimental and the analytical transfer function coincide, yields the story masses and story stiffness coefficients to be identified. This optimization procedure is conducted in MATLAB utilizing function *fminsearch* [28], where the square root of the sum of the squared errors between the resonance and anti-resonance frequencies of experimental and analytical transfer functions serves as objective parameter. As outcome, the following story masses and story stiffness coefficients are obtained,

$$\begin{aligned} &M_1 = 0.71\ \text{kg}, \quad M_2 = 0.75\ \text{kg}, \quad M_3 = 0.87\ \text{kg}, \\ &K_1 = 7271\ \text{N/m}, \quad K_2 = 13302\ \text{N/m}, \quad K_3 = 8423\ \text{N/m} \end{aligned} \tag{10}$$

The masses of the bottom plate $M_g = 3.6$ kg and the base plate $M_b = 3.5$ kg have been previously determined by weighing the individual assembly parts.

The objective for identification of Rayleigh coefficients η and β is that the magnitudes of the experimental and analytical transfer functions coincide at the natural frequencies in a least squares sense, yielding $\eta = 0.37\ \text{s}^{-1}$ and $\beta = 7 \cdot 10^{-6}$ s. Substituting these values and the parameters of Eq. (10) into Eq. (4) renders the elements of the damping matrix,

$$\begin{aligned} &c_{11} = 0.41, \quad c_{12} = c_{21} = -0.09, \quad c_{22} = 0.43, \\ &c_{23} = c_{32} = -0.06, \quad c_{33} = 0.38, \quad c_{1g} = c_{1b} = -0.05 \end{aligned} \tag{11}$$

As seen from Fig. 5(b), in the frequency range up to the third natural frequency the analytical transfer functions based on these structural parameters are in excellent agreement with the experimentally determined ones. Since the analytical model does not consider modes beyond the third mode (e.g. assuming massless columns, etc.), in the domain beyond the third natural frequency a difference between the analytical and experimental transfer functions becomes apparent. This does, however, not impair the effect of the considered hybrid control strategy, which aims at mitigating the response in the lower frequency domain.

3.2. Base-isolation subsystem

Stiffness coefficient K_b and damping coefficient C_b are the parameters to be identified. Although in the analytical model it is assumed that these parameters are constant, in reality they depend also on the weight of the structure above due to nonlinear effects such as friction etc. Thus, in the corresponding tests the three-story frame is dismounted and replaced by rigid steel bodies with equal mass as the frame, see Fig. 6(a). As such, the total mass of the test specimen above the bottom plate, $M_{tot} = M_b + \sum_{i=1}^{3} M_i$, remains the same. Note that the mass of the TLCD housing (100 g) is not considered here, since parameters of the solely base-isolated structure are sought. Since preliminary tests have shown that the base-isolation has some nonlinear properties, identification of the mechanical parameters of this subsystem is based on its free vibration response. Consequently, the horizontal motion capability of the bottom plates is deactivated by fixing the bottom plate with two angle brackets. This experimental setup exhibits essentially one DOF, whose linearized free vibrations are expressed through base displacement x_b [27],

$$\ddot{x}_b + 2\zeta_b \omega_b \dot{x}_b + \omega_b^2 x_b = 0 \tag{12}$$

with natural circular frequency ω_b and damping coefficient ζ_b of the base-isolation subsystem,

$$\omega_b = 2\pi f_b = \sqrt{K_b/M_{tot}}, \quad \zeta_b = C_b/(2M_{tot}\omega_b) \tag{13}$$

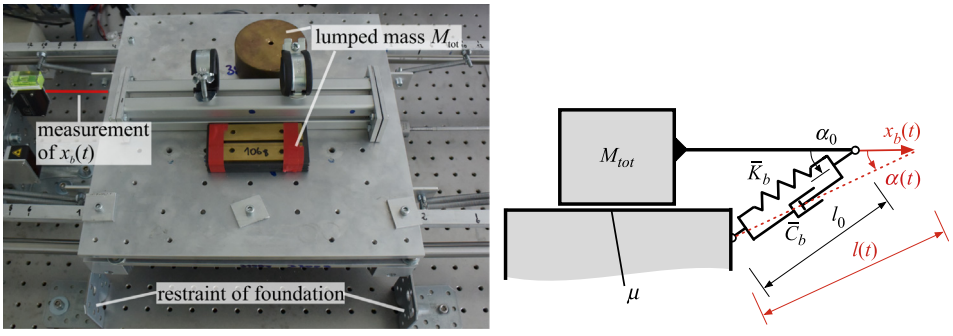

(a) Test setup (b) Nonlinear analytical model

Fig. 6. Parameter identification of the base-isolation subsystem.

The initial displacement of the base plate is imposed manually, and the induced free vibration response of the base plate recorded by laser sensor L2, see Fig. 1.

Although in the analytical model (according to Eq. (12)) commonly linear-elastic behavior is assumed, the experimental base-isolation setup is actually a slightly nonlinear device due to the displacement-dependent inclination angle of the springs. Another source of nonlinearity is friction of the linear bearings. The effects of these nonlinearities are apparent in the recorded free vibration responses induced by different initial displacements, shown in Fig. 7(a). In particular, when friction controls the response at small vibration amplitudes, nonlinear behavior is readily observed.

Fig. 6(b) shows a more realistic analytical model of the test setup, where the viscoelastic properties are lumped to an inclined *Kelvin-Voigt* element and friction is captured through *Coloumb* friction with coefficient μ between lumped mass M_{tot} and the foundation. Actual length $l(x_b)$ and inclination $\alpha(x_b)$ of the spring of the *Kelvin-Voigt* element depend on the base displacement $x_b(t)$ according to

$$l(x_b) = \sqrt{l_0^2 + x_b^2 + 2x_b l_0 \cos\alpha_0}, \quad \cos\alpha(x_b) = \frac{x_b + l_0\cos\alpha_0}{l(x_b)} \tag{14}$$

where l_0 is initial length and α_0 the initial inclination angle. In the equation of motion of this modified model,

$$M_{tot}\ddot{x}_b + F_{C,h}(x_b) + F_{K,h}(x_b) + \mu M_{tot} g \,\mathrm{sign}(\dot{x}_b) = 0 \tag{15}$$

the horizontal components of spring force $F_{K,h}(x_b)$ and damping force $F_{C,h}(x_b)$ are nonlinear due to the displacement-dependent inclination angle $\alpha(x_b)$,

$$F_{K,h}(x_b) = \overline{K}_b(l(x_b) - l_0)\cos\alpha(x_b), \quad F_{C,h}(x_b) = \overline{C}_b\dot{l}(x_b)\cos\alpha(x_b), \quad \dot{l}(x_b) = \dot{x}_b(x_b + l_0\cos\alpha_0)/l(x_b) \tag{16}$$

Variable g in Eq. (15) represents the acceleration of gravity, and sign(.) the signum function.

In the utilized identification procedure in the first step parameters $\overline{K}_b, \overline{C}_b$ and μ of this nonlinear model are determined, with $M_{tot} = 5.8$ kg, $\alpha_0 = 15^\circ$ and $l_0 = 0.09$ m. In this process, Eq. (15) is solved numerically for various initial displacements by MATLAB's standard solver for ordinary differential equations *ode45* [28]. Then, the sum of squared errors between the numerically simulated and the experimentally recorded responses $x_b(t)$ are minimized employing MATLAB function *fminsearch* [28], which yields the following parameters of the nonlinear model

$$\overline{K}_{b,opt} = 435 \text{ N/m}, \ \overline{C}_{b,opt} = 3.98 \text{ kg/s}, \quad \mu_{opt} = 0.003 \tag{17}$$

Additionally to the recorded response, Fig. 7(a) shows also the numerically derived counterparts based on these parameters. It is readily observed that the computed responses of the nonlinear analytical model matches excellently the recorded ones.

Since in engineering practice the numerical response prediction is commonly based on a linear analytical model of the hybrid-controlled structure as represented by Eq. (7), in the second step linearized dynamic properties of the base-isolation subsystem according to Eq. (13) are derived as $\omega_b = 8.36$ rad/s ($f_b = \omega_b/(2\pi) = 1.33$ Hz) and $\bar{\zeta}_b = 0.039$, with $K_b = \overline{K}_{b,opt}\cos^2\alpha_0 = 405$ N/m and $C_b = \overline{C}_{b,opt}\cos^2\alpha_0 = 3.71$ kg/s.

In Fig. 7(b), the red dotted line represents the free vibration response of the linear SDOF oscillator with these dynamic parameters assigned. Comparison with the corresponding output of the nonlinear model shows that frequency ω_b approximates well the actual periodicity of the nonlinear response. However, since the linear model disregards the effect of friction, it underestimates the energy dissipation, although the friction coefficient is small, i.e. $\mu_{opt} = 0.003$. Therefore, the linear damping coefficient ζ_b is adjusted (i.e. increased) by minimizing the squared errors between the nonlinear and the linear model output, yielding $\zeta_b = 0.068$. The linearized response based on these values, in Fig. 7(b) shown by the blue line with

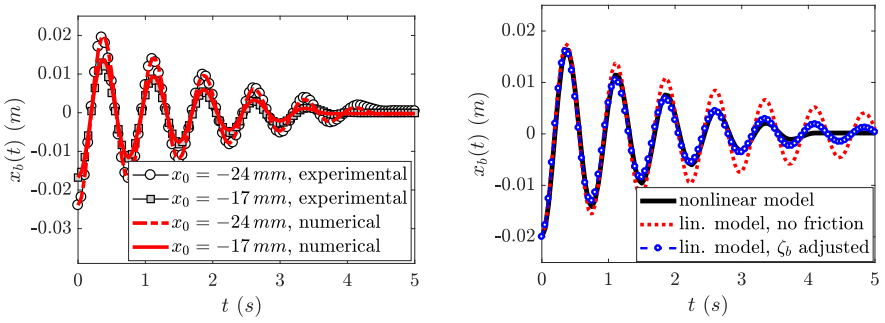

(a) Experimental versus nonlinear numerical response

(b) Nonlinear versus linearized numerical response

Fig. 7. Free vibration response of the base-isolation subsystem.

circular markers, captures sufficiently accurate the actual nonlinear response. However, it should be noted here that as such only the global energy dissipation capacity of this subsystem can be captured. The stick–slip motion due to friction at small vibration amplitudes, as observed in the experimental and nonlinear model outcomes, cannot be simulated by a viscous damper.

In summary, the identified parameters of the base-isolation subsystem, which enter Eq. (7), are

$$M_b = 3.5\ \text{kg}, \quad K_b = 405\ \text{N/m}, \quad C_b = 2\zeta_b\omega_b M_{tot} = 6.59\ \text{kg/s} \tag{18}$$

3.3. Tuned liquid column damper subsystem

In the underlying tests, the TLCD is attached to the base beam, while the base-isolation is deactivated and the frame dismounted, as depicted in Fig. 8(a). Three different TLCD setups are considered with different water mass, i.e. $m_l = 140$ g, $m_l = 150$ g respectively $m_l = 160$ g. Assuming linear vibrations according to Eq. 2, only the natural frequency ω_l and damping ratio ζ_l of the water column need to be identified. The considered TLCD setups are subjected to band-limited white noise base excitation $\ddot{x}_b \equiv \ddot{x}_g$, as described in Section 2.2.

During the experiments, the motion of the water surface and the displacement of a dot marked at the base beam (shown in Fig. 8(a)) are captured in full HD resolution with a frame rate of 60 *fps*, using a Nikon 1 J4 digital camera. The water surface motion is a representative quantity for the fluid column displacement y, and the recorded displacement of the dot corresponds to the ground displacement x_g. Since the camera is situated outside the test setup, both motion quantities are measured with respect to a fixed coordinate system. The recorded data are subjected to digital image processing. More specifically, motion tracking is accomplished by the Image Processing Toolbox functions implemented in MATLAB [30]. Calibration of the optical system is accomplished by measuring the distance between two distinct points (the dots on the base beam shown in Fig. 8(a)), both in the digital image and in the experimental setup, yielding a *mm*-to-pixel ratio. In the first step for each movie frame, image sections of the water surface are transformed into a black and white image using the MATLAB *im2bw* function. Then, the MATLAB *bwboundaries* function is applied to these images to capture the contour of the fluid surface. The center of the contour corresponds in the actual movie frame at time t to the fluid displacement coordinate $y(t)$. In parallel, the same procedure is applied to identify ground displacement x_g.

As an example, in Figs. 8(b) and (c) the recorded liquid surface is shown at two time instants. Green dashed lines indicate the tracked surface, and a circular marker its center. In the first case, the fluid motion is uniform, thus corresponding to the idealized model of a SDOF oscillator according to Eq. (2). In the latter case, liquid sloshing [31] can be observed. TLCD sloshing is a more local response phenomenon usually related to large amplitude and/or high frequency excitation, and thus, it does not significantly effect the (fundamental) frequency of the idealized fluid column.

Repeating this digital image processing procedure for all frames yields the time-history of $x_g(t)$ and $y(t)$. Based on these data, the experimental transfer function H_{YX_g} is computed, where the ground displacement $x_g(t)$ serves as input signal and column displacement $y(t)$ as output signal.

Fig. 9 shows experimentally obtained transfer functions H_{YX_g} in black lines with circular and square markers. Test results are presented for two excitation levels, characterized by the RMS ground displacement $\sigma^2_{X_g}$. For the results depicted on the left-hand side $\sigma^2_{X_g}$ is 0.5 mm, the outcomes shown on the right-hand are induced by seven times larger ground excitation, i.e. $\sigma^2_{X_g} = 3.5$ mm. Tests with larger excitation levels are not reasonable, because the water would spill out of the TLCD container. For each excitation level two tests with different liquid masses m_l are conducted, i.e. 140 g and 150 g for the lower excitation level, and 150 g and 160 g for the larger one. System identification reveals that the equivalent TLCD damping ratio is significantly affected by the excitation level. While for the first test series ζ_l is about 0.04, it increases to about 0.07 for larger excitation. This increase in apparent damping of the TLCD can be attributed to turbulence damping induced by higher liquid velocities at larger excitation levels. On the other hand, the fundamental TLCD natural frequency $\omega_l (= 2\pi f_l)$ is hardly

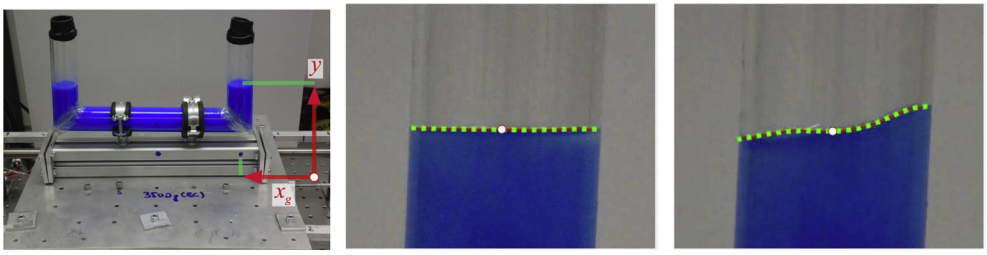

(a) Test setup and tracked coordinates (b) Uniform motion of the tracked liquid surface (c) Non-uniform motion of the tracked liquid surface

Fig. 8. Parameter identification for the TLCD subsystem.

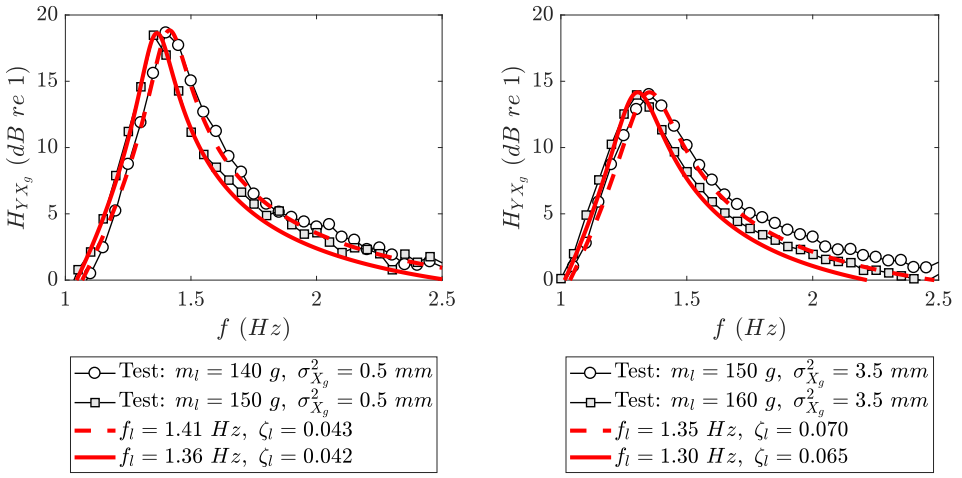

Fig. 9. Transfer function of the stand-alone TLCD for two different levels of ground excitation. Experimental outcomes and linearized SDOF model output.

Table 1
Identified parameters of the three considered TLCD configurations.

$m_l(g)$	m_l/M_{tot}	$f_l(Hz)$	ζ_l^{min}	ζ_l^{max}	$L_{eff}(m)$	α	ν
140	0.025	1.41	0.043	Not identified	0.25	0.80	1.07
150	0.026	1.36	0.042	0.070	0.27	0.75	1.03
160	0.028	1.30	Not identified	0.065	0.29	0.68	0.98

affected by the excitation amplitude, as both test results for $m_l = 150$ g have shown, i.e. $f_l = 1.36$ Hz and 1.35 Hz, respectively.

In Table 1 for each TLCD configuration liquid mass m_l, mass ratio m_l/M_{tot}, TLCD frequency f_l, identified equivalent TLCD damping ratio ζ_l, effective length of the water column length L_{eff}, geometry factor $\alpha = L_H/L_{eff}$, and frequency ratio $\nu = \omega_l/\omega_b(=f_l/f_b)$ are summarized. ζ_l^{min} corresponds to equivalent damping identified for excitation $\sigma^2_{\ddot{X}_g} = 0.5\,mm$, ζ_l^{max} represents damping values obtained for $\sigma^2_{\ddot{X}_g} = 3.5\,mm$. Note that L_{eff} has been derived from the relation $L_{eff} = 2g/\omega_l^2$, which follows from rearranging of ω_l according to Eq. (1).

Additionally, in Fig. 9 also the corresponding analytical transfer functions according to

$$\bar{H}_{YX_g}(f) = \frac{\alpha f^2}{f_l^2 + 2i\zeta f f - f^2} \tag{19}$$

are shown by red lines, using the identified parameters specified in Table 1. Expression 19 is the rearranged frequency domain representation of the linearized equation of motion of a base-excited TLCD, Eq. 2, considering that $\ddot{X}_g(f) = -(2\pi f)^2 X_g(f)$. Experimental and analytical transfer functions are in good agreement, which demonstrates that the SDOF approximation of the vibrations of the TLCD fluid column is sufficiently accurate.

4. Optimal TLCD parameters for the hybrid-controlled structure

In the corresponding analytical study [13], the TLCD parameters of such hybrid-controlled systems were optimized with respect to minimum relative base displacement $x_{b,rel} = x_b - x_g$, assuming (*i*) Gaussian white noise ground motion excitation, and (*ii*) that the structure above the base-isolation behaves rigid. With given parameters α, μ_l, ζ_b and ω_b, optimization can be narrowed down to finding optimal values for equivalent linear viscous damping ratio ζ_l and tuning frequency ratio ν. As derived in [13], this leads to minimization of the following smooth function

$$\begin{aligned}
&\phi(\nu,\zeta_l) = \frac{D_{ZX_b}}{N_Z} \quad \text{with}\\
&D_{ZX_b} = \zeta_l(1+\mu_l-\alpha^2\mu_l)^2 + \zeta_b\left[\alpha^4\mu_l^2 + 4\zeta_l^2(1+\mu_l)^2\right]\nu + \zeta_l^2(1+\mu_l)^2\left[4\zeta_b^2 + 3\alpha^2\mu_l + (4\zeta_l^2-2)(1+\mu_l)\right]\nu^2\\
&\qquad + \zeta_b^2(1+\mu_l)^2\left[\alpha^2\mu_l + 4\zeta_l^2(1+\mu_l)\right]\nu^3 + \zeta_l(1+\mu_l)^4\nu^4\\
&N_Z = \zeta_b\zeta_l + \zeta_l^2(4\zeta_b^2+\alpha^2\mu_l)\nu + 2\zeta_b\zeta_l\left[2\zeta_b^2 + \alpha^2\mu_l + (2\zeta_l^2-1)(1+\mu_l)\right]\nu^2 + \zeta_b^2\left[\alpha^2\mu_l + 4\zeta_l^2(1+\mu_l)\right]\nu^3 + \zeta_b\zeta_l(1+\mu_l)^2\nu^4
\end{aligned} \tag{20}$$

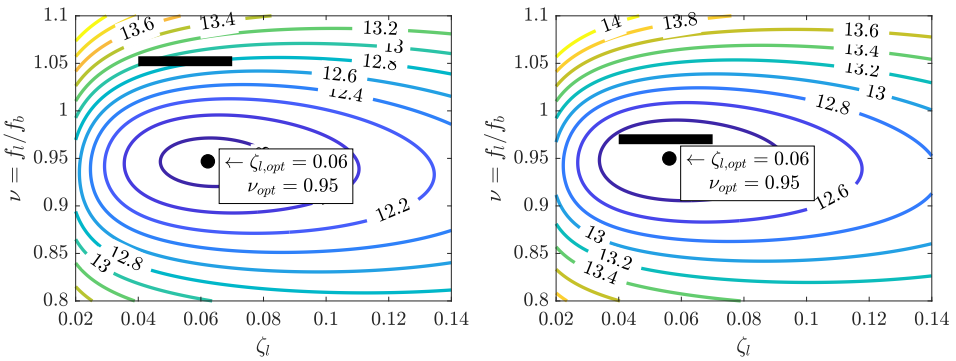

Fig. 10. Objective function $\phi(\nu, \zeta_l)$ for two TLCD setups, optimal control parameters, and experimentally identified parameter range of the control parameters (black bar).

Given the identified subsystem parameters α, ν_l and ζ_b specified in Table 1, evaluation of Eq. (20) over a range of damping ratios ζ_l and tuning frequency ratios ν yields a surface with a distinct minimum. As can be seen from Fig. 10, the optimum for the setups corresponds to the same parameter set $\zeta_{l,opt} = 0.06$ and $\nu_{opt} = 0.95$, although the shape of the surface $\phi(\nu, \zeta_l)$ is slightly different in each case. The experimentally observed range of the equivalent linear damping ratio $\zeta_l = 0.04 \ldots 0.07$ is indicated by a straight black line at the respective frequency ratios. It is readily observed that for the TLCD configuration $m_l = 140$ g frequency ratio ν is detuned by 13% from its optimal value $\nu_{opt} = 0.95$, 8% for $m_l = 150$ g, and 2% for $m_l = 160$ g. It can be, thus, concluded that the third TLCD setup with $m_l = 160$ g yields a control performance that is close to the optimal one, see Fig. 10(b). The two other setups, however, provide insight into the sensitivity with respect to detuning of the TLCD parameters.

5. Performance of the base-isolated and the hybrid-controlled structure

5.1. Base-isolated frame

To quantify the efficacy of the considered hybrid control strategy, initially the performance of the base-isolated frame without TLCD is investigated experimentally, subjected to band-limited white noise ground excitation in the frequency range $0.5 - 3$ Hz. The response of this structural configuration serves as benchmark solution. In accordance with the derivation of optimum tuning parameters in Section 4, the relative base displacement $x_{b,rel}(t) = x_b(t) - x_g(t)$ is the governing response parameter to be evaluated.

As outcome of this test, Fig. 11 shows the experimental transfer function obtained from input signal $\ddot{x}_g$ and the response signal $x_{b,rel}$. In the considered frequency range, this transfer function shows a distinct peak of $\max |H_{X_{b,rel}\ddot{X}_g}(f)| = 0.19\,s^2$, at frequency $f_1 = 1.34$ Hz. This first natural frequency of the base-isolated system is very close to the natural frequency of the base-isolation subsystem, i.e. $f_1 \approx f_b = 1.34$ Hz.

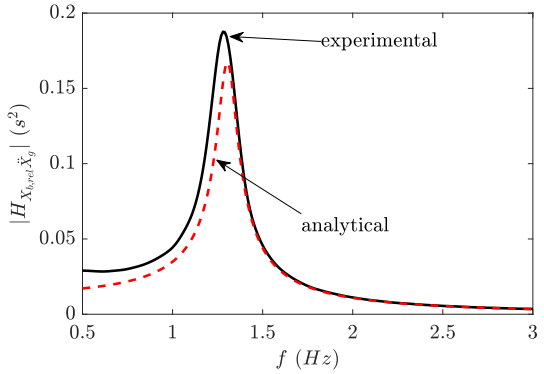

Fig. 11. Transfer function for the relative base displacement of the solely base-isolated shear frame. Experimental and analytical outcome.

Additionally, this figure shows also the corresponding transfer function of the analytical model, derived as

$$\bar{H}_{X_{b,rel}\ddot{X}_g}(f) = \frac{X_b(f) - X_g(f)}{\ddot{X}_g(f)} \tag{21}$$

where $X_b(f)$ and $X_g(f)$ are the base displacement respectively ground displacement in the frequency domain. The results of this figure reveal that the overall shape of the experimental transfer function is excellently approximated by the analytical model in the domain of the fundamental frequency. At lower frequencies deviations between both outcomes are apparent. The reason for this difference is the actual nonlinear behavior of the base-isolation in the experimental model, as discussed in Section 3.2.

To confirm this conclusion, additionally the free vibration response of the base-isolated system is computed, however, replacing the *Kelvin-Voigt* element of the linear analytical base-isolation subsystem model by the more realistic nonlinear model depicted in Fig. 6(b). Thus, when analyzing the response of the nonlinear analytical hybrid-controlled frame model, Eq. (5) must be replaced by

$$(M_b + m_l)\ddot{x}_b + \sum_{i=1}^{3} M_i \ddot{x}_i + F_{C,h}(t) + F_{K,h}(t) + \mu M_{tot} g \operatorname{sign}\dot{x}_b(t) = 0 \tag{22}$$

with internal forces $F_{C,h}(t)$ and $F_{K,h}(t)$ specified in Eq. (16). Imposing initial displacements $x_{b0} = 0.5$ mm and $x_{b0} = 3.5$ mm, respectively, substituting the identified parameters of the nonlinear base-isolation subsystem model summarized in Eq. (17) into Eq. (22), and numerical time integration of this equation in combination with Eq. (3) yields the base displacement prediction shown in Fig. 12 by full lines. The same initial conditions have been used in the underlying experiments for parameter identification of the base-isolation subsystem. For comparison, also the free vibration responses of the fully linear model is computed, employing the parameters specified in Eq. (18). The results are depicted in this figure with dashed lines.

The response of both models reveals the impact of friction on the response, in particular in the first case (i.e. $x_0 = 0.5$ mm) where the induced displacement amplitudes are small. For larger displacements, linear and nonlinear responses are in better agreement in the observed time frame, see Fig. 12(b). However, also in this case the difference between both response predictions becomes larger after the amplitudes decay to values as shown in the first numerical experiment. Note that for identification of the linearized base-isolation parameters in Section 3.2, free decay responses with initial displacements $x_0 = 17$ and 24 mm were used, respectively. It can be concluded that for small displacement amplitudes the impact of friction is omnipresent and the linearized model underestimates the energy dissipation. For moderate to large displacements, the linearized model serves as good compromise to describe the response behavior of the experimental model.

5.2. Hybrid-controlled frame

Subsequently, the dynamic behavior of the hybrid-controlled system is investigated, equipped with the three different TLCD configurations discussed in Section 3.3. To assess the effect of the TLCD on the dynamic performance of the structural system, the responses of the TLCD equipped setups are set in contrast to the benchmark solution of the solely base-isolated structure. Fig. 13 shows the experimental transfer functions for the relative base displacement of all considered structural configurations in the lower frequency range around the fundamental system frequency. It is readily observed that all TLCD configurations reduce the peak base displacement substantially with respect to the benchmark solution. As predicted, the TLCD with tuning frequency ratio $\nu = 0.98$ (i.e. $m_l = 160\,g$) exhibits the best performance. In this case, the maximum value of the transfer function in the range of the fundamental frequency is $\max|H_{X_{b,rel}\ddot{X}_g}(f)| = 0.08\,s^2$, which corresponds to a reduction of the maximum base displacement of 58% compared to the benchmark solution. For the TLCD with $\nu = 1.07$

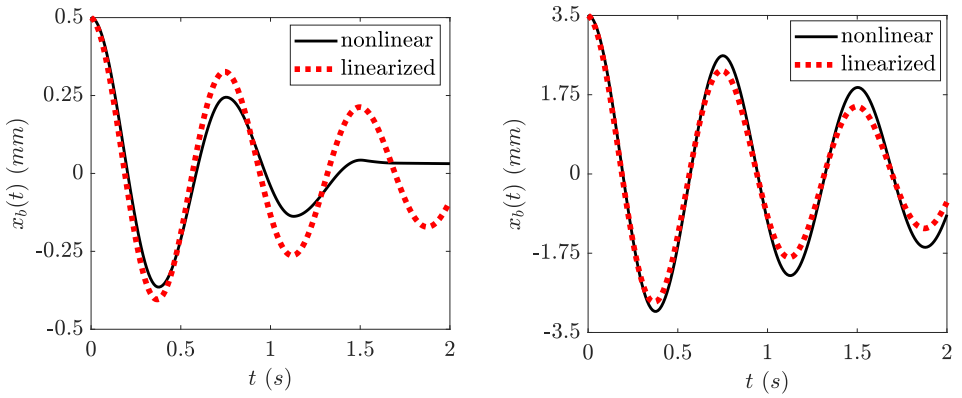

Fig. 12. Free vibration response of analytical models of the base-isolated structure. Nonlinear base-isolation model and linear model.

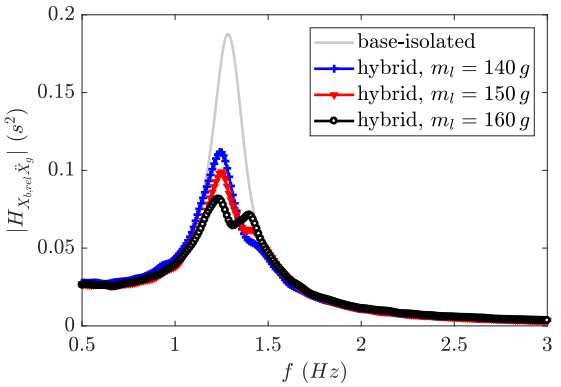

Fig. 13. Experimental transfer function for relative base displacement both of the solely base isolated and the hybrid-controlled frame with three different TLCD configurations.

($m_l = 140g$) the peak value $\max|H_{X_{b,rel}\ddot{X}_g}(f)|$ is 0.11 s^2, for the TLCD with 1.03 ($m_l = 150$ g) quantity $\max|H_{X_{b,rel}\ddot{X}_g}(f)|$ is 0.10 s^2. In the latter configurations the response reduction is 42% and 47%, respectively. This study gives also insight into the sensitivity of the proposed hybrid control strategy with respect to detuning. From the presented results it can be concluded that the application of a TLCD yields a performance gain of at least 40% compared to the solely base-isolated system, even for pronounced TLCD frequency ratio detuning up to 13% (i.e. $m_l = 140$ g).

The corresponding transfer functions of the analytical model according to Eq. (21) are also derived, solving the full set of Eq. (7) in the frequency domain due to force $F(f)$ and utilizing the identified parameters specified in Eqs. 10,11,18 and in Table 1. As outlined in Section 3.3, equivalent viscous damping of the TLCD depends on the excitation level. In the hybrid controlled setup, the corresponding level is given by the relative base displacement $x_{b,rel} = x_b - x_g$. Evaluating the standard deviation for the three presented TLCD configurations yields $\sigma^2_{X_{b,rel}} = 1.64$ mm for $m_l = 140g$, $\sigma^2_{X_{b,rel}} = 1.57$ mm for $m_l = 150$ g and $\sigma^2_{X_{b,rel}} = 1.50$ mm for $m_l = 160$ g. Assuming a linear variation of equivalent viscous damping with respect to the excitation level in the experimentally observed range yields an equivalent TLCD damping value of approximately $\zeta_l = 0.05$ for the three TLCD setups. Computations of transfer functions are conducted for the TLCD configurations $m_l = 140$ g and $m_l = 160$ g, which are shown in Fig. 14, set in contrast to corresponding experimentally obtained counterparts. For both TLCD configurations, in general a good agreement between the analytical and experimental outcomes is observed. The amplitudes show some minor deviations of a few percent. This difference is a result of the actual nonlinear behavior of the experimental control subsystems, as discussed previously. For on-site implementation, this difference is, however, insignificant, in particular, when comparing the response reduction of this hybrid-controlled systems with the solely base-isolated system. The peak values of experimental and analytical transfer function appear at the same frequency, proofing that the natural frequencies of the linear analytical model match excellently the ones of the experimental model.

In a final investigation, the effect of the hybrid control strategy on the acceleration response of the frame is assessed. To this end, the transfer function from input ground acceleration $\ddot{x}_g(t)$ to total top story acceleration $\ddot{x}_3(t)$ is evaluated experimentally, following tests with band-limited white noise in the frequency range up to 25 Hz. According to notation used in Section 3.1, the evaluated transfer function is denoted as $H_{\ddot{X}_3\ddot{X}_g}$, compare with Fig. 1. In Fig. 15(a), this transfer function

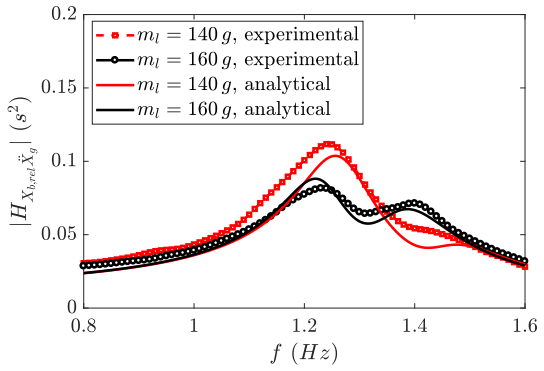

Fig. 14. Transfer functions for relative base displacement of the hybrid controlled system. Experimental versus analytical outcomes for two TLCD setups ($m_l = 140$ g and $m_l = 160$ g).

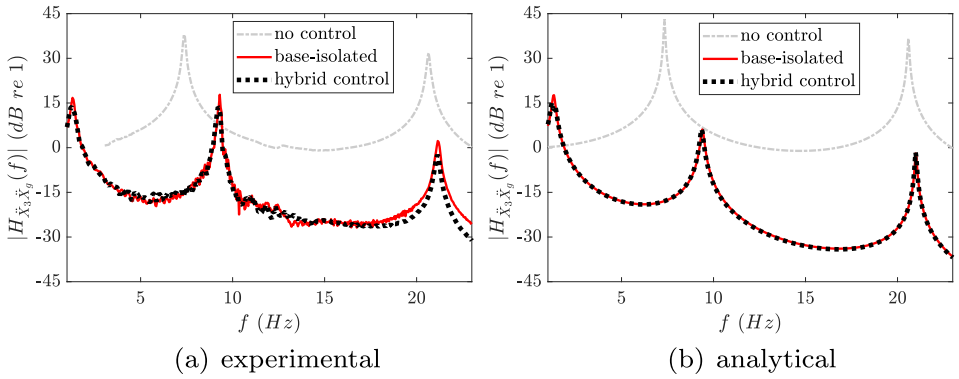

Fig. 15. Transfer functions for total top story acceleration of uncontrolled, solely base-isolated and hybrid-controlled frame.

is depicted for the solely base-isolated and for the hybrid-controlled frame with TLCD setup $m_l = 160$ g. For comparison, the corresponding transfer function of the uncontrolled frame is also included. As expected, adding the base-isolation to the frame, an additional natural frequency close to the natural frequency of the base-isolation subsystem becomes apparent, and the first natural frequency of the frame, $f_1 = 7.4$ Hz, is shifted to a value of about 9 Hz. As mentioned in Section 1, base-isolation acts as mechanical low-pass filter for the structure to be protected, which is confirmed by the amplitude reduction at the fundamental frequencies at 9 Hz and 21 Hz (note that a relative level shift of -20 dB represents an amplitude reduction by a factor 10). It is also observed that attaching the TLCD slightly reduces the peak value of this acceleration transfer function at the resonant frequencies. Thus, this hybrid control strategy not only reduces relative base displacement demand but also the total acceleration demand of the frame structure. In Fig. 15(b), corresponding analytical transfer functions are depicted utilizing the identified parameters specified in Eqs. 10,11,18 and in Table 1. They confirm the performance of the base-isolation in terms of amplitude reduction and resonance frequency shift. In contrast to the experimentally obtained transfer functions, a performance gain of the hybrid controlled structure is only visible at the fundamental frequency.

6. Conclusions

An innovative passive hybrid control strategy for reducing the response of buildings subjected to ground excitation was studied experimentally. In the considered control strategy, a tuned liquid column damper (TLCD) is installed at the base to reduce the dynamic displacement demand of a base-isolation subsystem. To this end, a small-scale experimental model was developed that can be adjusted easily to the needs of the conducted study. The characteristic dynamic parameters of the three subsystems of the model (i.e. the three-story frame, base-isolation, and TLCD) were identified separately. These parameters entered a corresponding analytical model of the test setup used to conduct comparative numerical studies of the effect of the TLCD. It was shown that slightly nonlinear behavior of the subsystems, which is always apparent in real structures, can be sufficiently accurately captured by a *linear* analytical model. However, these nonlinearities need to be carefully assessed beforehand. Additionally, a straightforward optimization procedure recently proposed by the authors has been validated experimentally. A further experimental study showed that detuning from the optimal TLCD frequency of 13% still leads to a reduction of the base displacement demand. The proposed hybrid control strategy was assessed based on experimentally determined transfer functions and their analytical counterparts. In summary, the outcomes of this experimental investigation support the conclusions that the proposed hybrid control strategy not only reduces the displacement demand of the base-isolation significantly, but also enhances the dynamic performance of the complete structural system.

Acknowledgment

Alberto Di Matteo and Antonina Pirrotta gratefully acknowledge the support received from the Italian Ministry of University and Research, through the PRIN 2015 funding scheme (project 2015 JW9NJT – Advanced mechanical modeling of new materials and structures for the solution of 2020 Horizon challenges).

References

[1] T.E. Saaed, G. Nikolakopoulos, J.-E. Jonasson, H. Hedlund, A state-of-the-art review of structural control systems, J. Vib. Control 21 (5) (2015) 919–937.
[2] J.M. Kelly, Base isolation: linear theory and design, Earthquake Spectra 6 (2) (1990) 223–244.
[3] M.C. Constantinou, T.T. Soong, G.F. Dargush, Passive energy dissipation systems for structural design and retrofit, Report MCEER-98-MN01, Multidisciplinary Center for Earthquake Engineering Research, 1998.
[4] A.C. Altunisik, A. Yetisken, V. Kahya, Experimental study on control performance of tuned liquid column dampers considering different excitation directions, Mech. Syst. Signal Process. 102 (2018) 59–71.

[5] F. Ziegler, The tuned liquid column damper as a cost-effective alternative for the mechanical damper in civil engineering structures, J. Acoust. Vibr. 12 (2007) 25–39.
[6] M.J. Hochrainer, F. Ziegler, Control of tall building vibrations by sealed tuned liquid column dampers, Struct. Control Health Monit. 13 (6) (2006) 980–1002.
[7] H.C. Tsai, The effect of tuned-mass dampers on the seismic response of base-isolated structures, Int. J. Solids Struct. 32 (8) (1995) 1195–1210.
[8] J.N. Yang, A. Danielians, S.C. Liu, Aseismic hybrid control systems for building structures, J. Eng. Mech. 117 (4) (1991) 836–853.
[9] B. Palazzo, L. Betti, Combined control strategies: base isolation and tuned mass damping, ISET J. Earthquake Technol. 36 (1999) 121–137.
[10] T. Taniguchi, A.D. Kiureghian, M. Melkumyan, Effect of tuned mass damper on displacement demand of base-isolated structures, Eng. Struct. 30 (12) (2008) 3478–3488.
[11] P. Xiang, A. Nishitani, Optimum design for more effective tuned mass damper system and its application to base-isolated buildings, Struct. Control Health Monit. 21 (1) (2014) 98–114.
[12] B. Khalid, F. Ziegler, A novel aseismic foundation system for multipurpose asymmetric buildings, Arch. Appl. Mech. 82 (10) (2012) 1423–1437.
[13] A. Di Matteo, T. Furtmüller, C. Adam, A. Pirrotta, The effect of tuned liquid column dampers on the seismic response of base-isolated structures, Acta Mech.https://doi.org/10.1007/s00707-017-1980-7.
[14] C. Adam, A. Hruska, M. Kofler, Elastic structures with tuned liquid column dampers, in: Proc. XVI IMEKO (International Measurement Confederation) World Congress, vol. VII, 2000, pp. 351–356.
[15] A. Di Matteo, F. Lo Iacono, G. Navarra, A. Pirrotta, Experimental validation of a direct pre-design formula for TLCD, Eng. Struct. 75 (2014) 528–538.
[16] A. Di Matteo, F. Lo Iacono, G. Navarra, A. Pirrotta, Optimal tuning of tuned liquid column damper systems in random vibration by means of an approximate formulation, Meccanica 50 (2015) 795–808.
[17] A. Di Matteo, F. Lo Iacono, G. Navarra, A. Pirrotta, Direct evaluation of the equivalent linear damping for TLCD systems in random vibration for pre-design purposes, Int. J. Non-Linear Mech. 63 (2014) 19–30.
[18] A. Di Matteo, F. Lo Iacono, G. Navarra, A. Pirrotta, Innovative modeling of tuned liquid column damper motion, Commun. Nonlinear Sci. Numer. Simul. 23 (2015) 229–244.
[19] A. Di Matteo, M. Di Paola, A. Pirrotta, Innovative modeling of tuned liquid column damper controlled structures, Smart Struct. Syst. 18 (1) (2016) 117–138.
[20] R.O. Ruiz, D. Lopez-Garcia, A.A. Taflanidis, Modeling and experimental validation of a new type of tuned liquid damper, Acta Mech. 237 (2016) 3275–3294.
[21] I. Takewaki, A. Der Kiureghian, M. Melkumyan, New experimental system for base-isolated structures with various dampers and limit aspect ratio, Earthquakes Struct. 5 (4) (2013) 461–475.
[22] L. Petti, G. Giannattasio, M. De Iuliis, B. Palazzo, Small scale experimental testing to verify the effectiveness of the base isolation and tuned mass dampers combined control strategy, in: The 14th World Conference on Earthquake Engineering, Beijing, China, 2008.
[23] A. Brandt, Noise and Vibration Analysis, John Wiley & Sons, 2011.
[24] M. Hochrainer, Control of Vibrations of Civil Engineering Structures with Special Emphasis on Tall Buildings (Ph.D. thesis), Vienna University of Technology, 2001.
[25] F. Ziegler, Mechanics of Solids and Fluids, Springer, Wien, 1999.
[26] J.B. Roberts, P.D. Spanos, Random Vibration and Statistical Linearization, Wiley, 1990.
[27] A. Chopra, Dynamics of Structures, fifth ed., Pearson, 2017.
[28] MATLAB version 9.2 (R2017a), Natick, Massachusetts: The MathWorks Inc., 2017.
[29] P.D. Welch, The use of Fast Fourier Transform for the estimation of power spectra: a method based on time averaging over short, modified periodograms, IEEE Trans. Audio Electroacoust. AU-15 (2) (1967) 70–73.
[30] The MathWorks Inc, Image Processing Toolbox User's Guide R2015b, 2015.
[31] R.A. Ibrahim, Liquid Sloshing Dynamics, Theory and Applications, Cambridge University Press, 2005.